Seasonality of spectral radiative fluxes and optical properties of Arctic sea ice during the spring-summer transition

Ran Tao[1,2], Marcel Nicolaus[1], Christian Katlein[1], Philipp Anhaus[1], Mario Hoppmann[1], Gunnar Spreen[2], Hannah Niehaus[2], Evelyn Jäkel[3], Manfred Wendisch[3], and Christian Haas[1,2]

[1] Alfred-Wegener-Institut Helmholtz-Zentrum für Polar- und Meeresforschung, Bremerhaven, Germany

[2] University of Bremen, Institute of Environmental Physics, Bremen, Germany

[3] Leipzig University, Leipzig Institute for Meteorology, Leipzig, Germany

* corresponding author: Ran Tao (ran.tao@awi.de)

Abstract

The reflection, absorption, and transmittance of solar (shortwave) radiation by sea ice play a crucial role in physical and biological processes in the ice-covered Arctic Ocean and atmosphere. These sea ice optical properties are of great importance, in particular during the melt season, as they significantly impact energy fluxes within and the total energy budget of the coupled atmosphere-ice-ocean system. In this paper, we analyse data from autonomous drifting stations to investigate the seasonal evolution of the spectral albedo, transmittance and absorptivity for different sea ice, snow, and surface conditions as measured during the MOSAiC expedition in 2019-2020. We find that the spatial variability of these quantities was small during spring, and that it strongly increased after the melt onset on May 26, 2020, when the liquid water content on the surface increased. The enhanced variability was then mostly determined by the formation of melt ponds. The formation of a single melt pond can increase the energy absorption of the sea ice by 50% compared to adjacent bare ice sites. The temporal evolution of the surface albedo and the sea ice transmittance was mostly event-driven and, thus, neither continuous nor linear. Furthermore, absorptivity and transmittance showed strong temporal and spatial variabilities, which depended on internal sea ice properties and under-ice biological processes and not only surface conditions. The spatial and temporal heterogeneity of sea ice conditions strongly impacted the partitioning of the solar short-wave radiation. This study shows that the formation and development of melt ponds can reduce albedo to 1/3, enhancing the total (summer) heat deposition. Individual ponding events can lead to more energy deposition than an earlier melt onset. The small-scale heterogeneity and the timing and duration of ponding events have to be considered when comparing (local) in-situ observations with large-scale satellite remote sensing datasets, and can help to improve numerical models.

Key points

- The transition of sea ice surface conditions from spring to summer is event-driven and neither continuous nor linear

- The summer energy budget of sea ice is more sensitive to melt pond evolution than to melt onset dates
- The seasonality of absorbed and transmitted radiation is not directly linked to the surface evolution
- The large variability between closely located stations can impact the large scale energy budget profoundly

1. Introduction

The surface energy budget of the Arctic summer ice cover is affected significantly by the observed decline of sea ice (e.g., Comiso et al., 2012., Nicolaus et al., 2012). The Arctic Sea ice showes an earlier melt onset and later freeze-up, thus a longer melt season. The small sea ice albedo during this period results in more solar radiative energy being absorbed by the sea ice and the ocean underneath (e.g., Comiso et al., 2012; Serreze and Stroeve, 2015; Stroeve and Notz, 2018). Sea-ice extent is shrinking (Serreze et al., 2015; Stroeve et al., 2014), thickness is decreasing (e.g., Haas et al., 2008; Kwok, 2018), and multi-year ice (MYI) is largely replaced by seasonal first-year ice (FYI) (e.g., Maslanik et al., 2011; Stroeve and Notz, 2018). Concurrently, the near-surface air temperature in the Arctic has increased two to three times more than the corresponding global mean surface temperature (e.g., Wendisch et al., 2022). The increasing air temperature provides more heat to melt the snow cover, resulting in decreasing albedo. Particularly, the transition from dry to wet snow results in a significant albedo decrease (Nicolaus et al., 2010; Perovich and Polashenski, 2012). The spatial and temporal variability of optical properties of the snow and sea ice such as albedo, transmittance and absorptivity increase after melt onset and subsequent melt pond formation (e.g., Perovich et al., 2002).

The melting snow increases the light transmittance and the amount of downwelling solar irradiance penetrating through the snow-covered sea ice, which impacts the physical and biological processes underneath the sea ice cover (e.g., Anhaus et al., 2021; Ardyna et al., 2020; Katlein et al., 2019; Perovich et al., 2008; Perovich and Richter-Menge, 2015). On the aggregate scale, approximately 8 % of the incident solar irradiance is transmitted into the ocean underneath in one year (Perovich 2005). The overwhelming amount (approximately 96 %) of the annually transmitted solar radiative energy penetrates through the sea ice layer during the four-month period from May to August when a sufficient amount of irradiance can be deposited on the surface with low albedo (Arndt and Nicolaus, 2014; Perovich 2005).

A detailed investigation of the temporal evolution and spatial variability of the surface and optical properties is needed to accurately represent the large-scale energy balance of the Arctic sea ice. Here, we present a dataset of spectral albedo and transmittance from 10 autonomous radiation measurement stations deployed during the MOSAiC expedition (Multidisciplinary Drifting Observatory for the Study of Arctic Climate) in 2019-2020 (Nicolaus et al., 2022). In-situ observations provide a detailed insight into the radiative partitioning in and through sea ice, which is otherwise inaccessible via satellite observation. We focus on the period from April 1 to July 18, 2020, when the Arctic sea ice transitioned from spring to summer. This paper identifies the seasonality and key events during this transition, examines the radiative partitioning during the transition period, and highlights their impact on the larger-scale energy balance.

2. Methods

2.1. The MOSAiC drift

The dataset presented in this study was obtained during the MOSAiC expedition (2019-2020) with the German research ice breaker *Polarstern* (Knust et al., 2017), following the Transpolar Drift (Nicolaus et al., 2022). The drift of *Polarstern* consisted of 3 phases:

(1) Drift 1 started in the Central Arctic at 85°N on October 4, 2019 and lasted until May 16, 2020, when *Polarstern* left the floe and paused the manned observation, while autonomous measurements continued.

(2) Drift 2 started on the same floe as Drift 1 on June 19, 2020, and lasted until July 31, 2020, when the floe disintegrated in the Fram Strait (78.9°N). Subsequently,

(3) Drift 3 started on a new floe near the North Pole (87.7°N) on August 21, 2020 and followed the Transpolar drift stream until September 20, 2020.

During the MOSAiC expedition, altogether 10 autonomous stations were deployed to measure spectral solar radiation fluxes above and under sea ice (Table 1). These radiation stations follow the concept described by Nicolaus et al. (2010b), and Figure 1 shows the drift track of the 10 radiation stations. The majority of the radiation stations (7) were installed during Drift 1 from October 5, 2019, to August 8, 2020, when the autonomous stations were recovered. The data collected during this period provide important observations covering the key spring-summer transition from May 16 to June 19, 2020, when no manned observations were possible due to the absence of *Polarstern* (between Drift 1 and 2). Furthermore, autonomous buoys 2020M29 and 2019S94 provide the evolution of air and surface temperature during the melt season.

Table 1. Operational times and metadata of all the autonomous radiation stations operated during the MOSAiC expedition. The 3 radiation stations in bold (2020R11 at the LM site, 2020R12 at the L3 site, and 2020R14 at the CO1 site) are discussed in detail in this study.

Station name	Site	Initial snow depth (m)	Initial ice thickness (m)	Deployment	First good data	Last good data	Failure/ recovery	Comment
2019R8	L1	0.18	0.78	Oct 05, 2019	Oct 6, 2019	Jun 13, 2020	Aug 06, 2020	Low sun elevation angle and hardware malfunction
2019R9	L2	0.10	0.30	Oct 07, 2019	Mar 13, 2020	Jun 12, 2020	Jun 17, 2020	Data interruption hardware malfunction
2020R10	CO1	0.07	1.49	Mar 08, 2020	Mar 13, 2021	Jul 20, 2020	Jul 21, 2020	Destroyed by ridge activity
2020R11	**LM**	**0.18**	**1.59**	**Mar 26, 2020**	**Mar 29, 2020**	**Jul 18, 2020**	**Aug 01, 2020**	
2020R12	**L3**	**0.08**	**1.67**	**Apr 24, 2020**	**Apr 24, 2020**	**Jul 22, 2020**	**Aug 08, 2020**	
2020R13	CO1	0.92	4.28	May 06, 2020	May 6, 2020	May 12, 2020	May 15, 2020	Destroyed by ridge activity
2020R14	**CO1**	**0.12**	**3.13**	**Apr 03, 2020**	**Apr 03, 2020**	**Jul 15, 2020**	**Jul 15, 2020**	
2020R15	CO2	0.01	1.52	Jul 12, 2020	Jul 13, 2020	Jul 19, 2020	Jul 19, 2020	Data interruption due to hardware malfunction
2020R21	CO3	0.35 (pond depth)	0.59	Aug 27, 2020	Aug 27, 2020	Sept 25, 2020	Nov 14, 2020	Deployed in a melt pond
2020R22	CO3	unknown	1.34	Aug 21, 2020	Aug 21, 2020	Sept 12, 2020	Sep 12, 2020	Data interruption due to hardware malfunction

2.2. Radiation station measurements and data processing

Each radiation station consisted of 3 RAMSES-ACC-VIS hyperspectral radiometers (TriOS GmbH, Rastede, Germany; Nicolaus et al., 2010b), measuring spectral irradiance from 320 nm to 950 nm with a spectral resolution of 3.3 nm. Measurement interval was 10 minutes. Figure 2 shows photos of both the above-ice and under-ice sensors. Above the ice, the upward-looking sensor measured incident (downwelling) irradiance ($E_{\mathrm{i}}(\lambda, \mathrm{t})$) and the downward-looking sensor measured reflected (upwelling) irradiance ($E_u(\lambda, \mathrm{t})$). The sensor installed under the ice measured the transmitted (downwelling) irradiance ($E_d(\lambda, \mathrm{t})$). The under-ice sensor was placed approximately 0.5 m below the ice bottom, measuring the transmitted irradiance through the sea ice, which can be covered with snow, surface scattering layer (bare ice), or liquid water (melt pond). During the observation time, the distance from the under-ice sensor to the ice bottom varied due to sea ice growth/melt.

The spectral irradiance above (upwelling and downwelling) and below (downwelling) the sea ice layer was recorded in counts per channel and then calibrated to absolute spectral irradiances (in W m^{-2} nm^{-1}) based on individual calibration files for each sensor (Nicolaus et al., 2010). The spectra were interpolated onto a 1 nm grid to calculate the ratios of spectral albedo, $\alpha(\lambda, \mathrm{t})$:

$$\alpha(\lambda, \mathrm{t}) = E_{\mathrm{u}}(\lambda, \mathrm{t}) / E_{\mathrm{i}}(\lambda, \mathrm{t}) \qquad (1)$$

and transmittance, $\tau(\lambda, \mathrm{t})$, as a ratio of E_{d} to E_{i}:

$$\tau(\lambda, \mathrm{t}) = E_{\mathrm{d}}(\lambda, \mathrm{t}) / E_{\mathrm{i}}(\lambda, \mathrm{t}) \qquad (2)$$

as a function of wavelength (λ) and time (t).

Nicolaus et al. (2010b) found insufficient data quality between 748 and 773 nm due to small E_i values resulting from Oxygen absorption around 760 nm. Hence, the albedo was linearly interpolated within this wavelength range.

The wavelength-integrated broadband albedo ($\alpha_{\mathrm{T}}(t)$) and transmittance ($\tau_{\mathrm{T}}(t)$) were calculated within the wavelength range of 350 nm to 920 nm via the following equations:

$$\alpha_{\mathrm{T}}(\mathrm{t}) = \frac{\int \alpha(\lambda,\mathrm{t})\mathrm{E}_i(\lambda,\mathrm{t})\mathrm{d}\lambda}{\int \mathrm{E}_i(\lambda,\mathrm{t})\mathrm{d}\lambda} \quad (3)$$

$$\tau_{\mathrm{T}}(\mathrm{t}) = \frac{\int \tau(\lambda,\mathrm{t})\mathrm{E}_i(\lambda,\mathrm{t})\mathrm{d}\lambda}{\int \mathrm{E}_i(\lambda,\mathrm{t})\mathrm{d}\lambda} \quad (4)$$

From the wavelength-integrated irradiances, we have calculated the following quantities:

(i) Net irradiance entering the sea ice, E_{ice} ,

$$E_{ice}(t) = E_{\mathrm{i}}(t) - E_{\mathrm{u}}(t) \quad (5)$$

(ii) Irradiance absorbed by the sea ice layer, E_a, and absorptivity, $\mathrm{abs}_{\mathrm{T}}(\mathrm{t})$:

$$E_a(t) = E_{\mathrm{i}}(t) - E_{\mathrm{u}}(t) - E_{\mathrm{d}}(t) \quad (6)$$

$$\mathrm{abs}_{\mathrm{T}}(\mathrm{t}) = 1 - \alpha_{\mathrm{T}}(\mathrm{t}) - \tau_{\mathrm{T}}(\mathrm{t}) \quad (7)$$

Note that the upward irradiance from the ocean to the sea ice bottom is omitted from the calculation as it may be assumed to be extremely small (ca. 1%) (Smith and Baker, 1981).

(iii) Sea ice melt rate ($\mathrm{m_{eq}}$) from the accumulated E_a and E_d over time through the surface and the ice:

$$m_{eq} = \frac{Q_A}{L_{melt} \cdot \rho_{ice}} \quad (8)$$

$$m_{eq} = \frac{Q_E}{L_{melt} \cdot \rho_{ice}} \quad (9)$$

where Q_A and Q_E is the absorbed and transmitted irradiance accumulated over time: $Q_A = \sum E_a \Delta t$ or $Q_E = \sum E_d \Delta t$, assuming the sea ice is at its melting point with a density $\rho_{ice} = 917$ kg m^{-3}, and a latent heat of melt L_{melt}= 0.3335 J kg^{-1}.

(iv) Albedo ratio ($\alpha(900)/\alpha(500)$) between the albedo at 900 nm ($\alpha(900)$) and the albedo at 500 nm ($\alpha(500)$). This ratio is sensitive to the liquid water content at the surface, thus an indicator of ponding, due to high absorption of water at 900 nm compared to 500 nm. The albedo ratio decreases from 1 as water accumulates at the surface.

(v) Transmittance ratio ($\tau(600)/\tau(450)$) between transmittance at 600 nm ($\tau(600)$) and transmittance at 450 nm ($\tau(450)$). This ratio is sensitive to the Chlorophyll-a content of the ice and upper ocean, and an increase may be used as an indicator for biological activities in or directly underneath sea ice (e.g., Ehn et al., 2008; Perovich et al., 1993).

(vi) We derive the wavelength of maximum transmittance of each spectrum as an indicator for the spectral shape that may be associated with biological influences, as used in Nicolaus et al. (2010a).

To investigate the long-term seasonality of apparent optical properties (i.e., albedo and transmittance), we used the maximum optical properties with reference to the maximum solar elevation angle. The daily mean irradiance was used to calculate E_d (Equation 5), E_a (Equations 6 and 7). Sub-diurnal variations and synoptic weather events are not resolved in the presented data.

2.3. Data quality and uncertainties

During the MOSAiC expedition, we deployed 10 autonomous spectral radiation stations on different sea ice and surface conditions. The stations were irregularly checked and maintained, but operated mostly independently. As with other autonomous instruments on drifting sea ice, some stations showed data interruption due to hardware failure (e.g., sensor or battery fault) or ice dynamics (e.g., ridging event) (as recorded in Table 1).

The above-ice radiation sensors were levelled and mounted on the rack, which was secured to the sea ice, a tilt due to the change of the surface or differential settling cannot be avoided during the long-term measurements in the dynamic sea ice regime. Hence, we monitored the inclination angle of the sensor over time, and excluded data with inclination angles larger than 10°. Additionally, we flagged the data as low quality when the solar elevation angle was smaller than 5°. Also, we observed some noise in spectral albedo at wavelength smaller than 400 nm, for the which might be due to the downward-looking sensor. A detailed description of the quality of the sensor and data interpolation, which was adopted in this study, can be found in Nicolaus et al. (2010b). Table 1 shows the operational time of each station and the resulting times with high-quality data.

Another uncertainty in this study comes from the distance between the under-ice sensor and the sea ice bottom. The initial set-up of approximately 0.5 m was to prevent sea ice growth from intruding the sensor. Due to the nature of autonomous stations, the distance changed over time with ice growth/melt without sensor depth adjustment. The observed transmitted irradiance included the absorption from the top water layer, resulting in a reduction of 20% to 30% of light transmittance (Nicolaus et al., 2010; Wozniak and Dera, 2007).

For quality control, we performed radiative transfer simulations for comparison with measured spectrally integrated E_i for all individual radiation stations during the measurement period. The modelling considered only cloudless atmospheric conditions, to avoid uncertainties caused by unknown cloud microphysical and macrophysical properties, which were not available for these remote radiation stations. However, a direct comparison for cloudless days allows (i) to monitor the occurrence of clouds, (ii) to identify potential effects of sensor misalignment in cloudless conditions, and (iii) a validation of the radiometric calibration. Broken cloud conditions can be identified by short-term variations of E_i, while more compact cloud situations lead to a general decrease of E_i compared to the simulations. Misalignment of the sensors can be detected by an asymmetric diurnal variation of E_i. The data were not corrected for this, but excluded from further analysis. In contrast to the cloud effects, uncertainties in the radiometric calibration would lead to systematic shifts in the measured E_i under cloud-free conditions compared to the simulations. However, this was not observed, indicating the stability of the radiometric calibration of the upward-looking sensor.

The simulations were performed with the library for radiative transfer routines and programs (libRadtran, Emde et al., 2016; Mayer and Kylling, 2005). As a solver for the radiative transfer equation, the Discrete Ordinate Radiative Transfer solver (DISORT) (Stamnes et al., 2000) was chosen. The extra-terrestrial spectrum was taken from Gueymard (2004). The meteorological input for the simulations was based on standard profiles of trace gas concentrations, air temperature, humidity, and pressure from Anderson et al. (1986).

The standard Sub-Arctic atmospheric profile was adapted to observations from radio soundings (Maturilli et al., 2021), which were launched about every six hours from *Polarstern*.

3. Results

3.1. Overview of surface properties and seasonality

Figures 3, 4, and 5 summarize the surface condition and seasonal evolution of optical properties for the observation period from May to mid-July, 2020. Figure 3 provides the time series of the measurements of the 10 radiation stations based on daily measurements at times of the highest solar elevation angle (local solar noon). Figure 4 shows photos of the surface conditions and radiation stations taken by autonomous cameras at the LM and L3 sites, and of the Central Observatory (CO) from a panorama camera (Panomax) onboard *Polarstern*. Figure 5 shows hourly values of meteorological parameters and a summary of the surface albedo evolution until the end of July. Figures 6, 7, and 8 show the seasonal evolution of spectral albedo and transmittance.

The dataset allows a particularly comprehensive analysis of the radiative fluxes of the Arctic sea ice during the spring-summer transition, a period that aligns with the maximum incoming irradiance. This study focuses on 3 radiation stations sited on multi-year ice (Table 1), which are later compared to satellite remote sensing observations. The 3 stations are named after their site of deployment hereinafter: LM, L3, and CO. Radiative fluxes showed an increasing spatial variability after the melt onset, mostly attributable to events (e.g., ponding and drainage, see Figure 4) which did not persist nor progress over the same time scale. This variability is well expressed in different phases and differences in timing and the sequence of events (similar to those defined by Nicolaus et al. (2010a) and Perovich et al. (2002)) in the different stations (Figures 3 and 4). Overall, we distinguished 3 phases of the sea ice and snow surface evolution when transitioning to the melt season:

(a) Phase 1 (before May 26) was characterized by the mostly below-freezing point air temperature (0°) and dry snow coverage at all 3 sites.
Melt onset occurred on May 26 (as also derived by Light et al. (2022)), when the air temperature remained above 0°C continuously for several days and snow started to melt on the surface.
(b) Phase 2 (May 26 to June 27) showed a strong surface spatial variability across the 3 sites due to events (e.g., ponding and drainage) at different times. The radiative fluxes reached their maximum during this phase.
(c) Phase 3 (after June 28) was characterized by the formation of a weathered surface layer, known as a scattering layer from the optical perspective. The spatial variability of surface properties between the 3 sites decreased compared to Phase 2.

3.2. Phase 1: Dry snow surface (before May 26)

Figure 5a shows that the air temperature reached the melting point (0°C) for two short intervals in April but regularly and for longer times after May 12. The surfaces of the three sites were covered by dry snow in April, e.g., Figures 4A and 4B.

From April 1 to May 25, the mean broadband albedo at all 3 sites was as high as 0.89 with a standard deviation of 0.03. Compared to later phases, the three sites had the most similar optical properties and most homogeneous surface conditions, although sea ice thickness and snow depth ranged from 1.59 m to over 3 m. The spectral albedo was higher than 0.80 over the entire wavelength range from 350 to 920 nm (e.g., Figure 7 shows the spectral albedo on May 1 at the LM and L3 sites). The mean albedo ratio was 0.87 (+/- 0.03) (Figure 3D).

The broadband transmittance was lower than 0.10 for all sites. The shape of spectral transmittance suggested no influence of biological activity centred around 490 nm (Figures 3E, 3F, and 8).

3.3. Phase 2: Melting snow and melt pond formation (May 26 to June 27)

Melt onset was detected on May 26 and snow started to melt on the surface (e.g., Figure 3D), as defined in Perovich et al., 2002. During Phase 2, the most prominent feature was the high spatial variability in the optical properties between the different sites. This variability is well expressed in differences in timing and the sequence of ponding events (MP1 at the LM site, MP2 at the L3 site, and MP3 again at the LM site).

Overall, the 3 sites showed a decrease in albedo at different scales due to melting snow and melt ponds (Figure 3A). The CO site showed a linearly decreasing broadband albedo and no ponding event. There were three individual ponds (MP1, MP2, MP3) that formed within the fields of view of the E_u sensors at the LM and L3 sites (e.g., Figures 4-E, 4-H, and 4-N). Events such as pond formation and later pond drainage increased the spatial variability of surface conditions during Phase 2. Also, the spectral albedo larger than 500 nm (the albedo ratio) showed a decrease due to the increasing liquid water on the surface (Figure 3D). The transmittance at the LM and L3 sites showed an increase and change in the spectral shape.

MP1: First melt pond on L3:

The first melt pond formed at L3 immediately after the melt onset (Figure 4E). Over at MP1, broadband albedo decreased to 0.58. The shape of the spectral albedo changed drastically from a rather linear- to a dome-shape, and the spectral albedo at a wavelength larger than 500 nm decreased below 0.67 (Figure 7, May 29). This resulted in the albedo ratio decreasing to 0.39. The broadband transmittance peaked at 0.08, and the wavelength of the maximum transmittance increased to 526 nm, compared to 496 nm during Phase 1 (Figure 3E).

On June 1, a thin new snow layer was observed (Figures 4F and 4G), and the L3 site showed an increase in broadband albedo to 0.87 and a decrease in broadband transmittance to 0.010. The shape of spectral transmittance showed a strong change (Figures 3E and 3F). On June 5, the maximum wavelength of transmittance increased to 576 nm, and the transmittance ratio peaked at 31.47, which aligns with the high absorption coefficient of under-ice biomass at wavelength centred around 440 nm (e.g., Lund-Hansen et all., 2015; Perovich et al., 1993). Compared to Phase 1 (May 1), the spectral transmittance on June 5 showed 2 strong decreases, each centred around 440 and 670 nm (Figure 8).

MP2: Melt pond on LM:

From June 5 onwards, mean broadband albedo decreased again with an increasing spatial variability (Figure 3A). The melt pond event (MP2, Figure 4H) at the LM site led to a decrease of its broadband albedo to 0.44. A strong decrease in albedo was found at wavelength larger than 550 nm, resulting in the minimum albedo ratio of 0.22 (Figure 3D). On June 14, a new snow layer increased the broadband albedo at the LM site for a day, and the albedo ratio increased temporally to 0.59.

The broadband transmittance at the LM site increased to 0.079. The shape of spectral transmittance showed a stronger variability (Figures 3C, 3E and 3F) after June 14, when the broadband transmittance started to decline from its maximum. For instance, on June 14, the transmittance ratio increased rapidly with the decreasing broadband transmittance and peaked at 16.0 (Figures 3F and 8A).

On June 17, the un-ponded L3 site showed a similar shape of spectral transmittance. The change in the shape of spectral transmittance persisted towards June 23, when the maximum wavelength of transmittance peaked at 710 nm, and the transmittance ratio peaked at 421 (Figures 3E and 3F).

MP3: Second melt pond on L3:

At the L3 site, a ponding event was again observed (e.g., Figure 4N), resulting in a minimum albedo of 0.38 on June 25, after a rapid decrease from 0.70 on June 23. The albedo ratio reached the minimum of 0.22 (e.g., Figure 7A).

Broadband transmittance remained lower than 0.012 during the formation of MP3. Compared to MP1 (also at the L3 site), even with the minimum albedo and more light being input into the ponded surface, the transmittance during MP3 was significantly lower than 0.080. The L3 site showed an absorptivity as high as 0.61 during MP3, compared to 0.34 during MP1. The spectral transmittance showed a similar spectral shape compared to June 23, with the maximum wavelength at 707 nm and a transmittance ratio of 77.0 (Figures 3E and 3F).

3.4. Phase 3: Advanced melt (after June 28)

From June 28 onwards, the 3 sites showed surface drainage and a weathered ice layer, resulting in a broadband albedo to show an increasing temporal consistency, and a more linear decline with less spatial variability (Figure 3C). From June 28 to July 18, the mean broadband albedo from all three sites was 0.69 (+/- 0.05) (Figure 3A). The spectral albedo showed a similar shape during this phase (e.g., Figure 8). The mean albedo ratio (Figure 3D), increased to 0.81 (+/- 0.02) on June 28, and then decreased to 0.73 (+/- 0.02) on July 15.

The broadband transmittance showed larger spatial variability, mainly attributed to the formation of a lead in the proximity of the L3 site (Figures 3C and 4T). At the L3 site, the spectral transmittance also showed a stronger change than the other 2 sites (Figure 8): e.g., two distinctive decreases centred around 440 nm and 670 nm were shown on June 28. On June 30 and July 5, the transmittance ratio at the L3 site showed two peaks at 57.8 and 29.5. At the LM site, the shape of spectral transmittance did not change as strongly, with the transmittance ratio of 0.6 and remained so until July 15 (Figures 3E and 3F).

Summarising the results of 3 individual time series, we find a general progression from spring to summer conditions with the broadband albedo ranging from 0.38 to 0.97 and transmittance from less than 0.010 to 0.120 across 3 sites. After the melt onset, we find an increasing surface variability from the 3 sites, particularly at the LM and L3 sites (compared to the CO site, which showed only a more linear evolution), driven by ponding events. Under the same atmospheric conditions, the timing and effects of events vary by site. Individual events, such as pond formation and drainage, new snow, and lead formation (e.g., Figure 4T), have effects, which lead to the short-term decrease of albedo, and an increase in absorptivity and transmittance. At the same site, the energy partitioning during different ponding events was different. For instance, the transmittance at the L3 site did not increase with the formation of MP3. We also examined the temporal evolution of the spectral albedo and transmittance, and distinguished the radiative fluxes into and through the snow and sea ice surface when the Arctic was transitioning from spring to summer.

3.5. Seasonality of the surface evolution and surface fluxes

Figure 9 shows the daily averaged broadband irradiances (incident, penetrating into the sea ice layer (Equation 5), absorbed by the ice layer (Equation 6), and transmitted through the ice layer) during the transition from spring to summer conditions. Figure 10 shows the daily mean of absorbed and transmitted irradiance of the 3 phases and individual events.

Phase 1 was characterized by the high albedo and increasing solar irradiance (e.g., Figures 5A and 5B). We computed the accumulated energy being deposited into the sea ice and snow surface (surface influx) during a 31-day period from April 25 to May 25, when all 3 sites were recording data. With the mean albedo of 0.89, the daily mean energy entering the snow and sea ice was smaller than 2 MJm^{-2} for all 3 sites. Although Phase 1 showed rather homogenous surface conditions at each site, compared to later phases, the energy budget differed between the sites. For instance, the LM site showed 35.6% (15 MJm^{-2}) more energy deposited into the surface of the L3 site.

After melt onset, the highest incident irradiance and surface influxes were observed (Phase 2). The 3 sites showed a mean surface influx of 3.7 (+/- 1.1) MJm^{-2} per day, almost twice as much as Phase 1. The LM site showed the highest surface influx (5 MJm^{-2}), mostly contributed by the 15-day duration of MP2. The L3 and CO sites showed a surface influx of 3.2 and 3.1 MJm^{-2}, respectively. During the ponding event of MP2, the LM site showed a daily surface influx of 7.2 MJm^{-2} (Figure 10B), ca. twice that of the L3 site during MP1 and MP3 (3.4 and 3.7 MJm^{-2}, respectively). As the surface melting progressed and the albedo decreased at all 3 sites, the impact of melt ponds (e.g., MP3) on increasing the surface influx became less. For instance, during the formation of MP3, the L3 site showed a surface influx of 3.7 MJm^{-2} per day, while the other 2 unponded sites both showed a mean surface influx of 3.2 MJm^{-2}.

Phase 3 is characterized by the weathered surface layer at the 3 sites after surface drainage. The mean surface influx increased to 4.0 (+/- 0.5) MJm^{-2}. The surface spatial variability between the 3 sites decreased during this phase. Also, a lead formed within 5 m of the L3 station, which increased the irradiance underneath the ice.

4. Discussion

4.1. Seasonality of energy deposition and melt rates

After melt onset, the surface influx increased at all sites, but not linearly or regularly. The strong spatial variability resulted from the very patchy surface evolution at the individual sites. During the melt season, absorptivity and transmittance varied between individual events (Sections 3.3. and 3.4.). The energy partitioning between in-ice absorptivity and transmission into the ocean varied significantly, impacting the primary internal ice melt rate.

After melt onset, the sea ice received the largest energy deposition, when the total absorbed irradiance by the ice and the top ocean layer was 120 (+/- 30) MJm^{-2}. Assuming bare ice at its melting point, the total absorbed irradiance during Phase 2 had the potential to melt 45.5 (+/- 11.7) cm of sea ice. The mean transmittance during this phase was 0.015, integrating to a total of 7.4 MJm^{-2}, a potential bottom melt of 2.8 cm.

The L3 site showed a total absorbed energy of 102.0 MJm^{-2} and total transmitted energy of 5.9 MJm^{-2} during the entire Phase 2. MP1 resulted in a total absorbed energy of 12.8 MJm^{-2} and transmitted energy of 2.8 MJm^{-2}. In late June, MP3 resulted in a total absorbed irradiance at the L3 site of 27.7 MJm^{-2} and the total transmitted energy only 0.2 MJm^{-2}. Computing the entire Phase 2 (34 days), the L3 site had the potential for internal and bottom ice melt of 38.7 cm and 2.0 cm, respectively.

During the entire Phase 2, the LM site showed the largest absorbed energy of 156.0 MJm^{-2} due to the formation of MP2, enough to melt 59.0 cm of ice. The transmitted energy was 15.5 MJm^{-2}, equivalent to 5.9 cm ice melt from the bottom. The ponding event (MP2) accounted for a significant portion of the total absorbed and transmitted energy of 97.0 and 9.7 MJm^{-2}, which had the potential to melt 36.7 cm and 3.7 cm ice internally and from the bottom, respectively.

During Phase 3, the 3 sites accumulated a mean absorbed energy of 60.3 MJm^{-2}, equivalent to a 22.8 cm internal ice melt. The transmitted energy showed a higher variability due to the lead formation near the L3 site (e.g., Figures 4 and 10B). Within 16 days, the L3 site accumulated a transmitted energy of 6.6 MJm^{-2}, enough to melt 2.5 cm ice.

Overall, the LM site by far showed the strongest absorption and ice melt. Although the L3 and CO sites showed a similar amount of energy deposition, the bottom melt rate of the L3 site was higher than the CO site. Having no ponding event, the CO site experienced a bottom melt rate of an order of magnitude smaller, as its transmittance remained a minimum.

4.2. Effects of melt ponds

In this study, we examined the energy partitioning of 3 sites with different snow, ice, and surface conditions during the spring-summer transition. Commonly, melt onset was on May 26, initiating a phase of strong spatial variability with little temporal consistency. As a result, the energy partitioning showed a strong variability, driven by melt pond formation and drainage at different sites and with different timing.

The locations of melt ponds depend on surface topography. Melt ponds from the previous year have the potential to pre-condition the location and size of new melt ponds (Thielke et al., 2022; Webster et al., 2022). However, at the time of installation of the stations, it was not foreseeable if or even when ponds might form in the field of view of the E_u sensor, which has a footprint of only 1 m^2. As a result, the described optical properties and melt pond evolution is not necessarily representative for a region larger than the field of view of the RAMSES sensors. Having consistent results for the 3 long-term stations, we find the same characteristics during the 3 phases. This is also supported by other stations, e.g., 2020R10 (Figure 3A), also showed a ponding event and minimum albedo observation in mid-June, similar to MP2 at the LM site.

The 3 stations in this study were at multi-year ice and representative of similar ice conditions. There was an increasing surface spatial variability over a floe scale, starting in late May. The melt pond fraction increased to over 20% in late June (Webster et al., 2022), followed by a temporary decrease due to drainage. Based on measurements from the 3 radiation stations, we defined Phase 3 with a start date in late June. However, the surface drainage was not homogeneous for the entire ice floe. In July, the melt pond fraction increased and reached the maximum (Webster et al., 2022).

4.3. Representativeness of radiation station measurements

In this study, we focused on 3 stations that succeeded in capturing the spring summer transition in 2020 as planned. They were on multi-year ice. The evolution of the LM and L3 sites was strongly impacted by partly abrupt changes in melt pond conditions, and thus strongly event-driven. Compared to this, the CO site showed a rather linear seasonal progression, but also had the thickest ice.

However, the result is representative for multi-year ice with similar conditions, not the entire ice floe. We were not able to obtain measurements on thin ice, which melted completely in July. Considering the peak solar irradiance, there would be a large amount of energy deposited into the ice and the ocean via the thin ice when transitioning into the summer. Taking into account the expanding and deepening of melt ponds from mid-June (Webster et al., 2022) and later pond drainage (e.g., Light et al., 2022) over a larger floe-size scale, the surface heterogeneity can impact the energy budget of sea ice during the melt season and can alter the location of sea ice melt.

Furthermore, the MOSAiC ice floe showed a thinner ice thickness compared to the surrounding and historical records along the same trajectory (Krumpen et al., 2020; Krumpen et al., 2021). This indicated an earlier melt onset and earlier melt pond formation (Krumpen et al., 2021). Figure 11A shows the melt onset date of the MOSAiC stations to satellite data. Compared to the satellite record, the MOSAiC melt onset showed an early melt onset (May 26) for its latitude (6th percentile).

Also, a lead was formed within 5 metres of L3 site in July, which increased the observed transmitted irradiance as the light was scattered horizontally. The surface albedo at the L3 site was unaffected. Such event could not represent the pure physical evolution of radiative fluxes of sea ice, but only a single unrepresentative case.

This study provides insights of the spectral albedo and transmittance of different sea ice types, which is important to understand the solar partitioning over an aggregate scale. We recommend future work to expand this result to a larger area (e.g., aerial images) to improve sea ice classification, and to extend the observation period. This will require a wider range of ice conditions, in particular including this and melting ice.

4.4. Comparison to earlier studies

Figure 11 compares the seasonality of melt onset date and albedo of the MOSAiC observation to the Tara and SHEBA expeditions (Nicolaus et al., 2010a; Perovich et al., 2002) as well as with satellite remote sensing data from 1998 to 2020. Having multiple stations, we are able to investigate the seasonality, and more importantly, the scale spatial variability of radiative partitioning during this period.

The best comparable dataset is from the Tara expedition (Nicolaus et al., 2010a), which is based on a radiation station with the same set-up and sensors as in this study. The Tara station was deployed on 2 m thick ice and snow and drifted from 88.2°N on April 29 to 87.8°N on August 1, 2007. Nicolaus et al. (2010a) derived a melt onset on June 10, 15 days later than during MOSAiC. After the melt onset, the Tara albedo first showed an almost linear decrease until reached its minimum on July 1, and the surface drainage occurred on July 3. The mean surface influx transitioned from 45.5 to 54.5 Wm^{-2} during this period (Nicolaus et al., 2010a). During the according phase (Phase 2) of the MOSAiC observation, the mean surface influx ranged from 35.4 (CO site) to 58.1 Wm^{-2} (LM site). The LM site also showed a higher mean absorbed and transmitted irradiance than the Tara station. The maximum transmittance showed a linear increase at the Tara station, reached its maximum (0.66) on July 1. Compared to the MOSAiC station, the LM and L3 sites showed a higher maximum transmittance at an earlier date, due to melt pond events in late May and mid-June. Overall, the LM and L3 sites showed a similar seasonality to the Tara station, whilst the CO site showed lower solar fluxes as it was on thicker ice.

The SHEBA experiment drifted in the Beaufort and Chukchi Seas, from 76°N in April to 78 °N at the end of July 1998 (Perovich et al., 1998). It represents sea ice conditions at lower latitudes 20 years earlier. The SHEBA melt onset was 3 days later, on May 29 (Perovich et al., 2002). We extracted 2 points from its albedo line to show the evolution of a bare ice surface and melt pond. After the melt onset, the albedo showed a steady decrease until June 13, when the albedo started to decrease more strongly with higher spatial variability. With the melt pond darkening, a maximum albedo of 0.18 was reached by the end of July. Beyond that, during the entire extent of the SHEBA observation, the minimum albedo of 0.1 was reached in mid-August *(Perovich, 2002).* On the other hand, the MOSAiC dataset (e.g., the L3 site) showed an increasing surface spatial variability directly after the melt onset date.

The MOSAiC data set stands out for having multiple stations that monitor radiative fluxes above and under sea ice of different ice conditions, but with the same atmospheric forcing. As a result, our measurements describe a broader range of radiative fluxes of sea ice than a single time series, highlighting variability. This variability is particularly important when the ice is transitioning into the melt season, with peak solar irradiance, and more energy deposition into the sea ice with a higher spatial variability.

5. Conclusions

In this study, we present the seasonal evolution of radiation fluxes during the spring-summer transition during the MOSAiC expedition in 2019/2020. They provide spectral radiative fluxes on and through different sea ice, snow, and surface conditions during most of the sunlit period. We focus on the seasonal progression during the spring-summer transition by investigating 3 radiation stations, with a continuous record from April 1 to July 18, 2020.

With results from multiple stations, we identified 3 phases:

(i) Phase 1: dry snow surface before melt onset on May 26. The three sites were characterised by high albedo and small radiative net influx with a small spatial variability.

(ii) Phase 2: melting snow and melt pond formation. After melt onset, the air temperature was positive for several days and melting snow increased the liquid water content at the surface. Phase 2 showed the strongest spatial variability due to ponding events (MP1, MP2, and MP3). Different from the previously defined seasonality (e.g., Nicolaus et al., 2010a; Perovich et al., 2002), which separated ‘melting snow’ and ‘melt pond formation’. Phase 2 showed a mixture of surface evolution of reoccurring ponding events (e.g., L3 site) and melting snow over sea ice (e.g., CO site). The evolution of net surface influx during Phase

2 was mostly event-driven and neither linear nor continuous. Ponding events might not directly increase light transmittance but absorptivity.

(iii) Phase 3: after melt pond drainage on June 29. The three sites showed a steadily decreasing albedo and less variability in the absorptance of the radiative fluxes. However, the transmitted irradiance at the L3 site peaked due to the lead formation in its proximity, which enhanced the bottom melt rate by an order of magnitude compared to Phase 2.

Having multiple observation stations, we are able to investigate the solar partitioning of different ice surface conditions. We found that the summer energy budget of sea ice depends more on melt pond evolution than on melt onset dates. For instance, a single ponding event (e.g., MP2) accounted for as high surface influx than the unponded CO site during the entire Phase 2. The strong spatial variability between different ice types and surface conditions can impact the large-scale energy budget.

The time series shows strong spatial and temporal variations. On the spatial scales of kilometres, as used for general circulation models (GCM) or satellites, melt onset is usually defined as one specific date for the area. Our radiation stations show that the earliest detected melt is not a good predictor for the large-scale melt onset and that locations with the longest melting season (in our case L3) are not necessarily experiencing the strongest accumulated net surface flux and ice melt over the season (which in our case was the LM site). Therefore, the high spatial and temporal variability we found needs to be taken into account when interpreting larger scale Arctic-wide datasets.

Data availability

The MOSAiC radiation stations data are available on Pangaea (Tao et al., 2022, https://doi.pangaea.de/10.1594/PANGAEA.949556). The ice mass balance station 2020M29 can be accessed on https://data.meereisportal.de, and the Snow Buoy 2019S94 is published on Pangaea (Nicolaus et al., 2020, https://doi.org/10.1594/PANGAEA.925325).

Acknowledgements

This work was carried out, and data used in this manuscript were produced as part of the international Multidisciplinary drifting Observatory for the Study of the Arctic Climate (MOSAiC) with the tag MOSAiC20192020. We thank all persons involved in the expedition of the research vessel Polarstern during MOSAiC in 2019–2020 (AWI_PS122_00) as listed in Nixdorf et al. (2021). We highly acknowledge the contribution by Ilkka Matero, Julia Regnery, Jan Rohde, Jakob Belter, Steven Fons, Igor Sheikin, Alexey Niubom, David Clemens-Sewall for deploying and/or recovering the radiation stations.

Funding

This work was funded by the German Federal Ministry of Education and Research (BMBF) through financing the Alfred-Wegener-Institut Helmholtz-Zentrum für Polar- und Meeresforschung (AWI) and the Polarstern expedition PS122 under the grant N-2014-H-060_Dethloff, the AWI through its projects: AWI_ROV, AWI_ICE, and AWI_SNOW. The AWI buoy program was funded by the Helmholtz strategic investment Frontiers in Arctic Marine Monitoring (FRAM).

R.T. was funded by the Deutsche Forschungsgemeinschaft (DFG, German Research Foundation) – Project-ID 268020496 – through the Transregional Collaborative Research Centre TRR-172 “ArctiC Amplification: Climate Relevant Atmospheric and SurfaCe Processes, and Feedback Mechanisms (AC)^3 “.

P.A. was funded through the Alfred-Wegner-Institutes internal project AWI_ROV, through the German Ministry of Education and Research (BMBF) project MOSAiC 3 - IceScan (03F0916A), and additional funds through the project DiatomARCTIC (03F0810A), part of the Changing Arctic Ocean Programme, jointly funded by the UKRI Natural Environment Research Council (NERC) and the BMBF.

References

Anderson, M., A. C. Bliss, and S. Drobot. 2019. Snow Melt Onset Over Arctic Sea Ice from SMMR and SSM/I-SSMIS Brightness Temperatures, Version 4. [Indicate subset used]. Boulder, Colorado USA. NASA National Snow and Ice Data Center Distributed Active Archive Center. https://doi.org/10.5067/A9YK15H5EBHK. [Date Accessed].

Anderson, G., Clough, S., Kneizys, F., Chetwynd, J., and Shettle, E.: AFGL atmospheric constituent profiles (0-120 km), Tech. Rep. AFGL-TR-86-0110, Air Force Geophys. Lab., Hanscom Air Force Base, Bedford, Mass., 1986.

Anhaus P, Katlein C, Nicolaus M, Arndt S, Jutila A and Haas C (2021) Snow Depth Retrieval on Arctic Sea Ice Using Under-Ice Hyperspectral Radiation Measurements. Front. Earth Sci. 9:711306. doi: 10.3389/feart.2021.711306

Ardyna, M., Mundy, C.J., Mayot, N., Matthes, L.C., Oziel, L., Horvat, C., Leu, E., Assmy, P., Hill, V., Matrai, P.A., Gale, M., Melnikov, I.A. and Arrigo, K.R. (2020). Under-Ice

Phytoplankton Blooms: Shedding Light on the ‘Invisible’ Part of Arctic Primary Production. *Frontiers in Marine Science*, 7. doi:10.3389/fmars.2020.608032.

Arndt, S. and Nicolaus, M. (2014). Seasonal cycle and long-term trend of solar energy fluxes through Arctic sea ice. *The Cryosphere*, 8(6), pp.2219–2233. doi:10.5194/tc-8-2219-2014.

Comiso, J.C. (2012). Large Decadal Decline of the Arctic Multiyear Ice Cover. *Journal of Climate*, 25(4), pp.1176–1193. doi:10.1175/jcli-d-11-00113.1.

Ehn, J.K., Mundy, C.J. and Barber, D.G. (2008). Bio-optical and structural properties inferred from irradiance measurements within the bottommost layers in an Arctic landfast sea ice cover. *Journal of Geophysical Research*, 113(C3). doi:10.1029/2007jc004194.

Emde, C., Buras-Schnell, R., Kylling, A., Mayer, B., Gasteiger, J., Hamann, U., Kylling, J., Richter, B., Pause, C., Dowling, T. and Bugliaro, L. (2016). The libRadtran software package for radiative transfer calculations (version 2.0.1). *Geoscientific Model Development*, 9(5), pp.1647–1672. doi:10.5194/gmd-9-1647-2016.

Gueymard, C.A. (2004). The sun’s total and spectral irradiance for solar energy applications and solar radiation models. *Solar Energy*, 76(4), pp.423–453. doi:10.1016/j.solener.2003.08.039.

Haas, C., Pfaffling, A., Hendricks, S., Rabenstein, L., Etienne, J.-L. and Rigor, I. (2008). Reduced ice thickness in Arctic Transpolar Drift favors rapid ice retreat. *Geophysical Research Letters*, 35(17). doi:10.1029/2008gl034457.

Katlein, C., Arndt, S., Belter, H.J., Castellani, G. and Nicolaus, M. (2019). Seasonal Evolution of Light Transmission Distributions Through Arctic Sea Ice. *Journal of Geophysical Research: Oceans*, 124(8), pp.5418–5435. doi:10.1029/2018jc014833.

Knust, Rainer (2017). Polar Research and Supply Vessel POLARSTERN operated by the Alfred-Wegener-Institute. *Journal of large-scale research facilities JLSRF* 3. https://doi.org/10.17815/jlsrf-3-163.

Krumpen, Thomas, Florent Birrien, Frank Kauker, Thomas Rackow, Luisa von Albedyll, Michael Angelopoulos, H. Jakob Belter, et al. 2020. 'The MOSAiC Ice Floe: Sediment-Laden Survivor from the Siberian Shelf'. *The Cryosphere* 14 (7): 2173–87. https://doi.org/10.5194/tc-14-2173-2020.

Krumpen, Thomas, Luisa von Albedyll, Helge F. Goessling, Stefan Hendricks, Bennet Juhls, Gunnar Spreen, Sascha Willmes, et al. 2021. 'MOSAiC Drift Expedition from October 2019 to July 2020: Sea Ice Conditions from Space and Comparison with Previous Years'. *The Cryosphere* 15 (8): 3897–3920. https://doi.org/10.5194/tc-15-3897-2021.

Kwok, R. (2018). Arctic sea ice thickness, volume, and multiyear ice coverage: losses and coupled variability (1958–2018). *Environmental Research Letters*, 13(10), p.105005. doi:10.1088/1748-9326/aae3ec.

Lund-Hansen L. C., Markager S., Hancke K., Stratmann T., Rysgaard S., Ramløv H., & Sorrell B. K. (2015). Effects of sea-ice light attenuation and CDOM absorption in the water below the Eurasian sector of central Arctic Ocean (>88°N). *Polar Research*, *34*. https://doi.org/10.3402/polar.v34.23978

Maslanik, J., Stroeve, J., Fowler, C. and Emery, W. (2011). Distribution and trends in Arctic sea ice age through spring 2011. *Geophysical Research Letters*, 38(13), p.n/a-n/a. doi:10.1029/2011gl047735.

Maturilli, M., Holdridge, D.J., Dahlke, S., Graeser, J., Sommerfeld, A., Jaiser, R., Deckelmann, H., Schulz, A., 2021. Initial radiosonde data from 2019-10 to 2020-09 during project MOSAiC, Alfred Wegener Institute, Helmholtz Centre for Polar and Marine Research, Bremerhaven. PANGAEA. https://doi.org/10.1594/PANGAEA.928656

Mayer, B. and Kylling, A. (2005). Technical note: The libRadtran software package for radiative transfer calculations - description and examples of use. *Atmospheric Chemistry and Physics*, 5(7), pp.1855–1877. doi:10.5194/acp-5-1855-2005.

Nicolaus, M., Gerland, S., Hudson, S.R., Hanson, S., Haapala, J. and Perovich, D.K. (2010a). Seasonality of spectral albedo and transmittance as observed in the Arctic Transpolar Drift in 2007. *Journal of Geophysical Research*, 115(C11). doi:10.1029/2009jc006074.

Nicolaus, M., Hoppmann, M., Lei, R., Belter, H. J., Fang, Y.C., and Rohde, J. (2020): Snow height on sea ice, meteorological conditions and drift of sea ice from autonomous measurements from buoy 2019S94, deployed during MOSAiC 2019/20. Alfred Wegener Institute, Helmholtz Centre for Polar and Marine Research, Bremerhaven, PANGAEA, https://doi.org/10.1594/PANGAEA.925325

Nicolaus, M., Hudson, S.R., Gerland, S. and Munderloh, K. (2010b). A modern concept for autonomous and continuous measurements of spectral albedo and transmittance of sea ice. *Cold Regions Science and Technology*, 62(1), pp.14–28. doi:10.1016/j.coldregions.2010.03.001.

Nicolaus, M., Katlein, C., Maslanik, J. and Hendricks, S. (2012). Changes in Arctic sea ice result in increasing light transmittance and absorption. *Geophysical Research Letters*, 39(24). doi:10.1029/2012gl053738.

Nicolaus, M., Perovich, D.K., Spreen, G., Granskog, M.A., von Albedyll, L., Angelopoulos, M., Anhaus, P., Arndt, S., Belter, H.J., Bessonov, V., Birnbaum, G., Brauchle, J., Calmer, R., Cardellach, E., Cheng, B., Clemens-Sewall, D., Dadic, R., Damm, E., de Boer, G. and Demir, O. (2022). Overview of the MOSAiC expedition: Snow and sea ice. *Elementa: Science of the Anthropocene*, 10(1). doi:10.1525/elementa.2021.000046.

Perovich, D.K. (2005). On the aggregate-scale partitioning of solar radiation in Arctic sea ice during the Surface Heat Budget of the Arctic Ocean (SHEBA) field experiment. *Journal of Geophysical Research: Oceans*, 110(C3). doi:10.1029/2004jc002512.

Perovich, D.K., Cota, G.F., Maykut, G.A. and Grenfell, T.C. (1993). Bio-optical observations of first-year Arctic sea ice. *Geophysical Research Letters*, 20(11), pp.1059–1062. doi:10.1029/93gl01316.

Perovich, D.K. and Elder, B. (2002). Estimates of ocean heat flux at SHEBA. *Geophysical Research Letters*, 29(9), pp.58–158–4. doi:10.1029/2001gl014171.

Perovich, D.K. and Polashenski, C. (2012). Albedo evolution of seasonal Arctic sea ice. *Geophysical Research Letters*, 39(8), p.n/a-n/a. doi:10.1029/2012gl051432.

Perovich, D.K. and Richter-Menge, J.A. (2015). Regional variability in sea ice melt in a changing Arctic. *Philosophical Transactions of the Royal Society A: Mathematical, Physical and Engineering Sciences*, 373(2045), p.20140165. doi:10.1098/rsta.2014.0165.

Perovich, D.K., Richter-Menge, J.A., Jones, K.F. and Light, B. (2008). Sunlight, water, and ice: Extreme Arctic sea ice melt during the summer of 2007. *Geophysical Research Letters*, 35(11). doi:10.1029/2008gl034007.

Perovich, D.K., Roesler, C.S. and Pegau, W.S. (1998). Variability in Arctic sea ice optical properties. *Journal of Geophysical Research: Oceans*, 103(C1), pp.1193–1208. doi:10.1029/97jc01614.

Serreze, M.C. and Stroeve, J. (2015). Arctic sea ice trends, variability and implications for seasonal ice forecasting. *Philosophical Transactions of the Royal Society A: Mathematical, Physical and Engineering Sciences*, 373(2045), p.20140159. doi:10.1098/rsta.2014.0159.

Smith, R.C., and Baker, K.S., "Optical properties of the clearest natural waters (200–800 nm)," Appl. Opt. 20, 177-184 (1981), https://doi.org/10.1364/AO.20.000177

Stamnes, K., Tsay, S.-C., Wiscombe, W., and Laszlo, I.: DISORT, A General-Purpose Fortran Program for Discrete-Ordinate-Method Radiative Transfer in Scattering and Emitting Layered Media: Documentation of Methodology, Tech. Rep., Dept. of Physics and Engineering Physics, Stevens Institute of Technology, Hoboken, NJ 07030, 2000.

Stroeve, J. and Notz, D. (2018). Changing state of Arctic sea ice across all seasons. *Environmental Research Letters*, 13(10), p.103001. doi:10.1088/1748-9326/aade56.

Stroeve, J.C., Markus, T., Boisvert, L., Miller, J. and Barrett, A. (2014). Changes in Arctic melt season and implications for sea ice loss. *Geophysical Research Letters*, 41(4), pp.1216–1225. doi:10.1002/2013gl058951.

Tao, R., Anhaus, P., Arndt, S., Belter, H.J., Hoppmann, M., Katlein, C., Matero, I., Regnery, J., Rohde, J., and Nicolaus, M. (2022). Spectral radiation fluxes, albedo and transmittance from autonomous measurements, deployed during MOSAiC 2019/20. Alfred Wegener Institute, Helmholtz Centre for Polar and Marine Research, Bremerhaven, PANGAEA, https://doi.org/10.1594/PANGAEA.949556 (in review)

Thielke, L., Fuchs, N., Spreen, G., Tremblay, B., Birnbaum, G., Huntemann, M., Hutter, N., Itkin, P., Jutila, A. and Webster, M.A. (2022). Seasonal predictability of summer melt ponds from winter sea ice surface temperature. doi:10.1002/essoar.10512617.1.

Webster, M.A., Holland, M., Wright, N.C., Hendricks, S., Hutter, N., Itkin, P., Light, B., Linhardt, F., Perovich, D.K., Raphael, I.A., Smith, M.M., von Albedyll, L. and Zhang, J. (2022). Spatiotemporal evolution of melt ponds on Arctic sea ice. *Elementa: Science of the Anthropocene*, 10(1). doi:10.1525/elementa.2021.000072.

Wendisch, M., M. Brückner, S. Crewell, A. Ehrlich, J. Notholt, C. Lüpkes, A. Macke, J. P. Burrows, A. Rinke, J. Quaas, M. Maturilli, V. Schemann, M. D. Shupe, E. F. Akansu, C. Barrientos-Velasco, K. Bärfuss, A.-M. Blechschmidt, K. Block, I. Bougoudis, H. Bozem, C. Böckmann, A. Bracher, H. Bresson, L. Bretschneider, M. Buschmann, D. G. Chechin, J. Chylik, S. Dahlke, H. Deneke, K. Dethloff, T. Donth, W. Dorn, R. Dupuy, K. Ebell, U. Egerer, R. Engelmann, O. Eppers, R. Gerdes, R. Gierens, I. V. Gorodetskaya, M. Gottschalk, H. Griesche, V. M. Gryanik, D. Handorf, B. Harm-Altstädter, J. Hartmann, M. Hartmann, B. Heinold, A. Herber, H. Herrmann, G. Heygster, I. Höschel, Z. Hofmann, J. Hölemann, A. Hünerbein, S. Jafariserajehlou, E. Jäkel, C. Jacobi, M. Janout, F. Jansen, O. Jourdan, Z. Jurányi, H. Kalesse-Los, T. Kanzow, R. Käthner, L. L. Kliesch, M. Klingebiel, E. M. Knudsen, T. Kovács, W. Körtke, D. Krampe, J. Kretzschmar, D. Kreyling, B. Kulla, D. Kunkel, A. Lampert, M. Lauer, L. Lelli, A. von Lerber, O. Linke, U. Löhnert, M. Lonardi, S. N. Losa, M. Losch, M. Maahn, M. Mech, L. Mei, S. Mertes, E. Metzner, D. Mewes, J. Michaelis, G. Mioche, M. Moser, K. Nakoudi, R. Neggers, R. Neuber, T. Nomokonova, J. Oelker, I. Papakonstantinou-Presvelou, F. Pätzold, V. Pefanis, C. Pohl, M. van Pinxteren, A. Radovan, M. Rhein, M. Rex, A. Richter, N. Risse, C. Ritter, P. Rostosky, V. V. Rozanov, E. Ruiz Donoso, P. Saavedra-Garfias, M. Salzmann, J. Schacht, M. Schäfer, J. Schneider, N. Schnierstein, P. Seifert, S. Seo, H. Siebert, M. A. Soppa, G. Spreen, I. S. Stachlewska, J. Stapf, F. Stratmann, I. Tegen, C. Viceto, C. Voigt, M. Vountas, A. Walbröl, M. Walter, B. Wehner, H. Wex, S. Willmes, M. Zanatta, and S. Zeppenfeld, **2023**: Atmospheric and Surface Processes, and Feedback Mechanisms Determining Arctic Amplification: A Review of First Results and Prospects of the (AC)^3 Project, *Bull. Amer. Meteorol. Soc.,* **104 (1), E208–E242, https://doi.org/10.1175/BAMS-D-21-0218.1**

Wendisch, M., Müller, D., Schell, D. and Heintzenberg, J. (2001). An Airborne Spectral Albedometer with Active Horizontal Stabilization. *Journal of Atmospheric and Oceanic Technology*, 18(11), pp.1856–1866. doi:2.0.co;2">10.1175/1520-0426(2001)018<1856:aasawa>2.0.co;2.

Wozniak, B. and Dera, J. (2007). *Light Absorption in Sea Water*. Springer Science & Business Media.

Figures

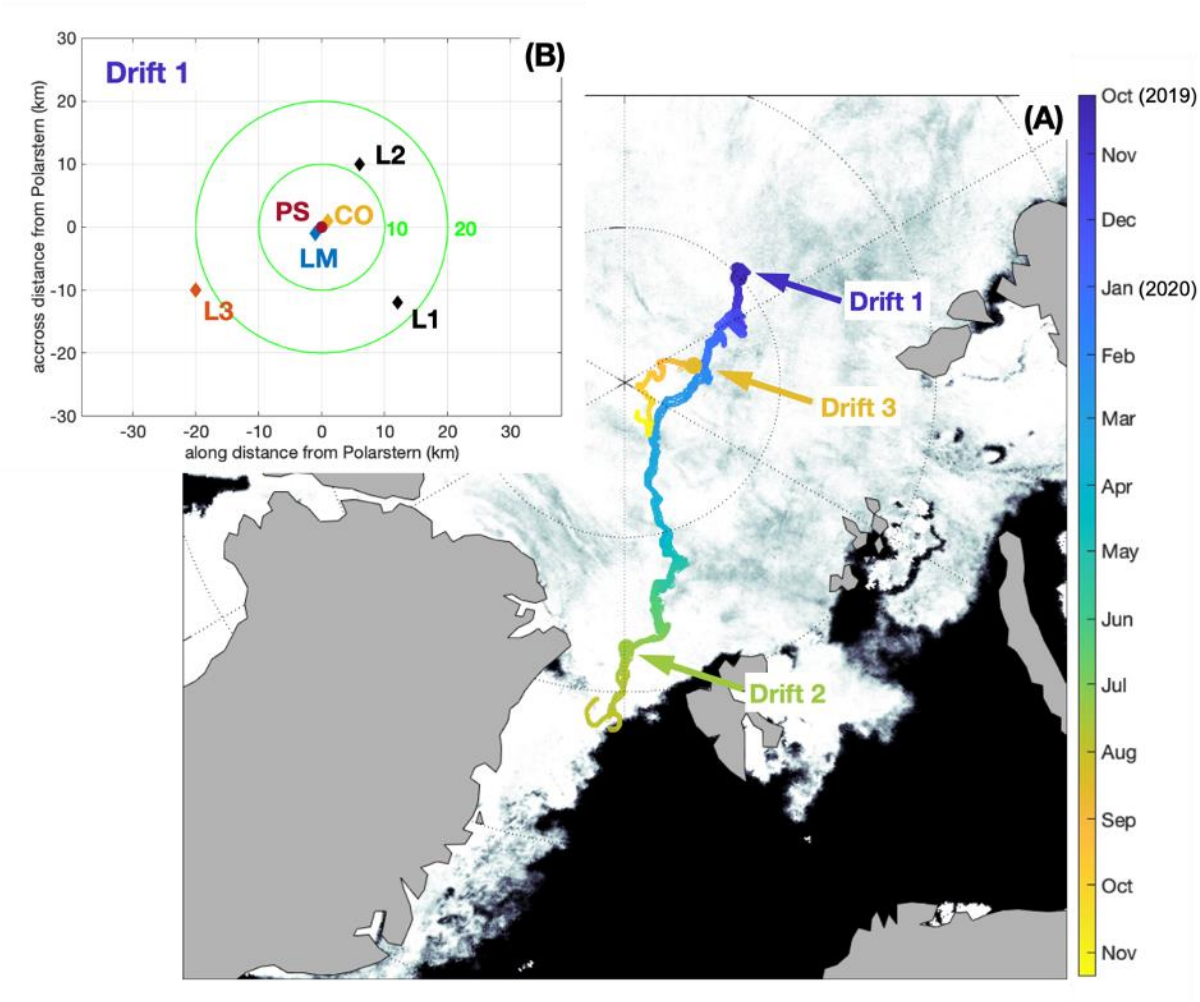

Figure 1. Drift tracks, distribution of sites, and sea ice concentration. (A) Drift tracks of the radiation stations from October 2019 to November 2020. The starting point of Drift 1, 2 and 3 are labelled accordingly. The background shows the sea ice concentration retrieved via AMSR2 (Advanced Microwave Scanning Radiometer 2) on May 25, 2020. (B) Relative positions of the Distributed Network sites (L1, L2, L3, LM) at the beginning of Drift 1, centered around *Polarstern* (PS) and the Central Observatory (CO).

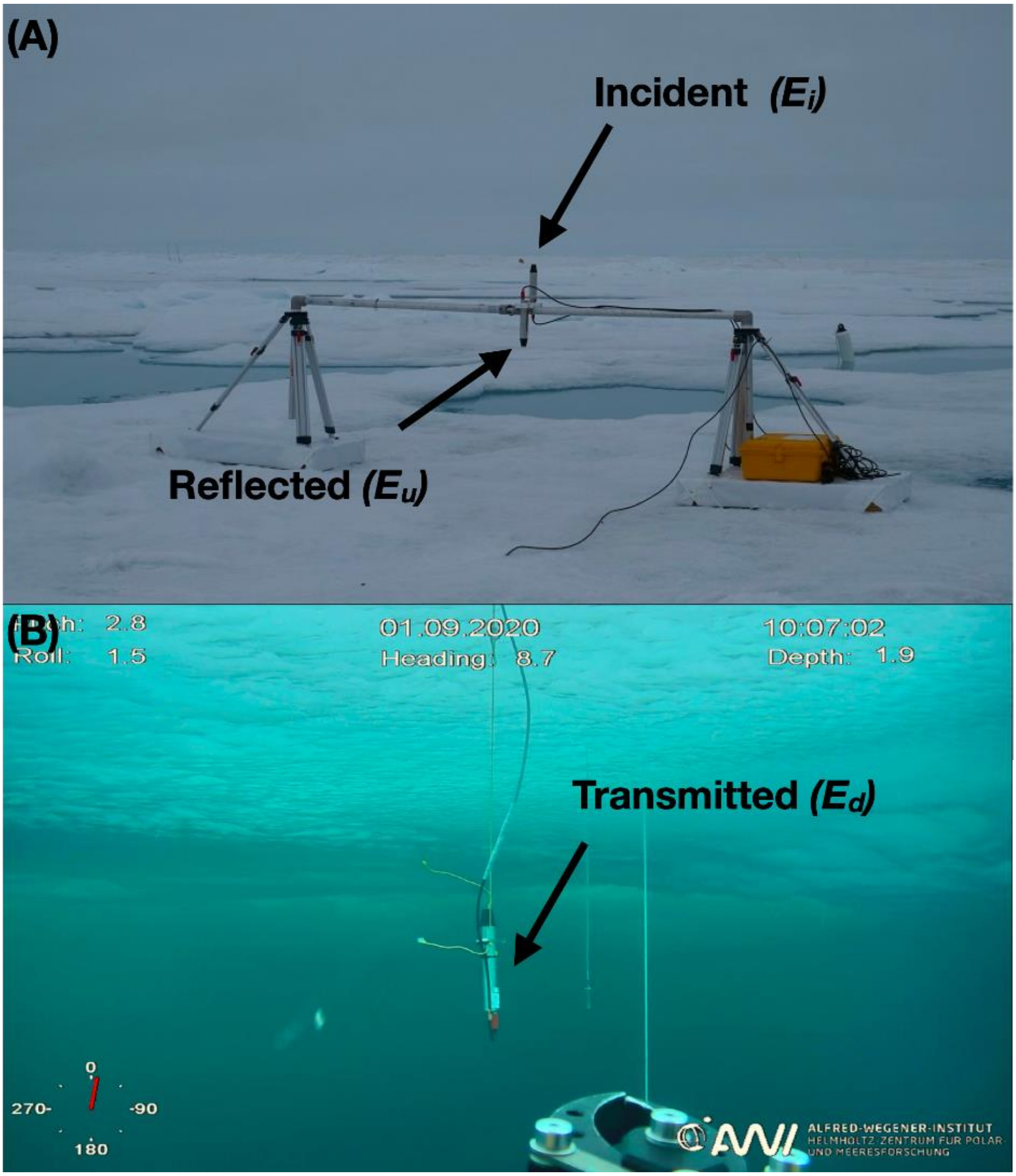

Figure 2. Photos of a radiation station set-up on and under sea ice. (A) Photograph of station 2020R15 on July 18, 2020, including the sensors for incident and reflected irradiance, (B) photograph of station 2020R21 on September 01, 2020, showing the sensor for transmitted irradiance hanging under the ice. The photo was taken from a Remotely Operated Vehicle. Labels give attitude parameters of the vehicle.

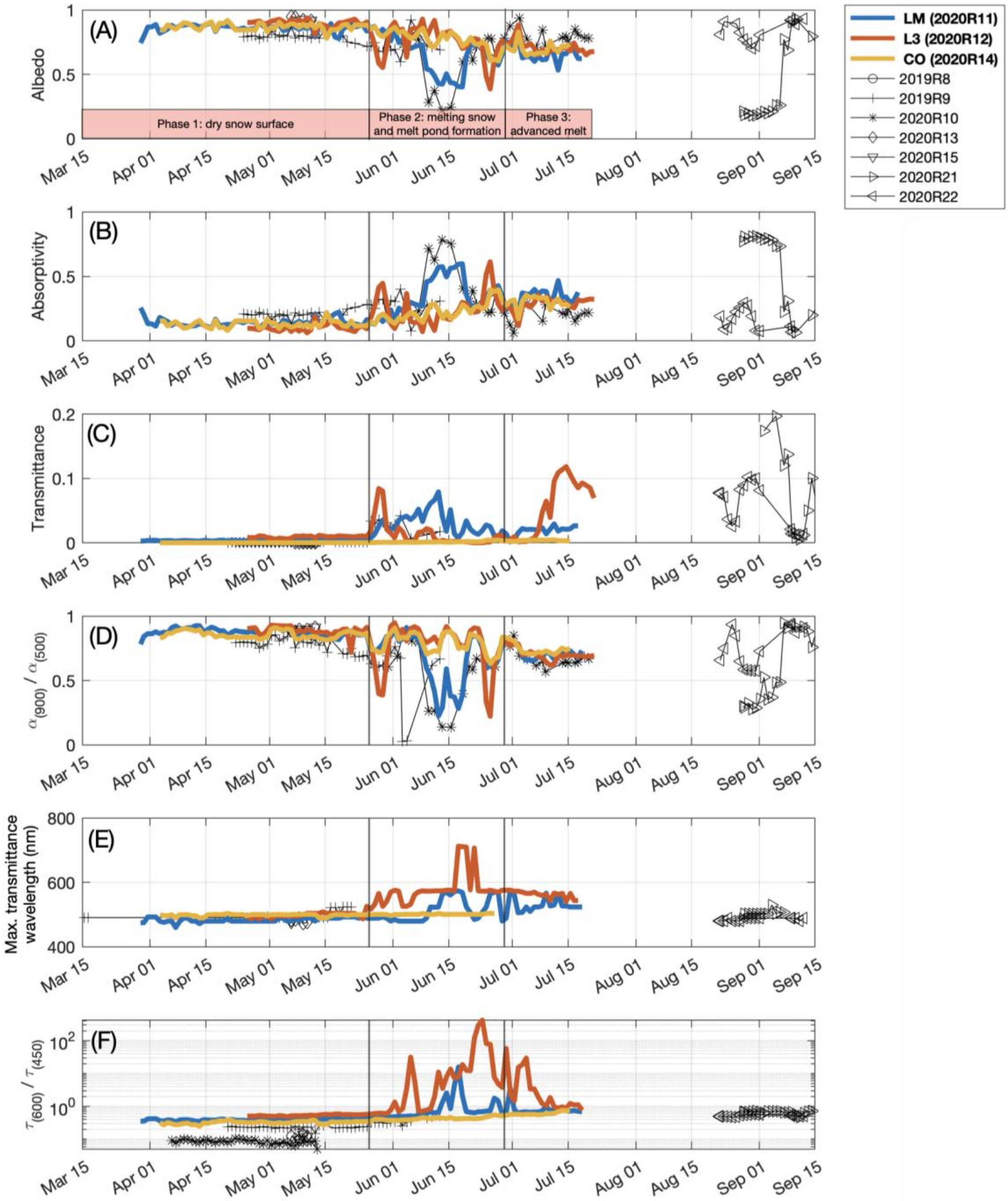

Figure 3. The seasonal progression of optical properties measured by radiation stations during the sunlit season in 2020. Lines show wavelength-integrated (350-920 nm) values of (A) surface albedo, (B) surface and ocean absorptivity, (C) transmittance, (D) Albedo ratio of 900 to 500 nm ($\alpha(900)/\alpha(500)$), (E) Wavelength of the maximum transmittance of each spectrum, and (F) Transmittance ratio at 600 to

450 nm (*τ(600)/ τ(450)).* The three main radiation stations are highlighted in color: 2020R11 at the LM site, 2020R12 at the L3 site, and 2020R14 at the CO site. The two black vertical lines indicated the melt onset (May 26) and stage of advanced melt and the formation of surface weathered layer (June 28).

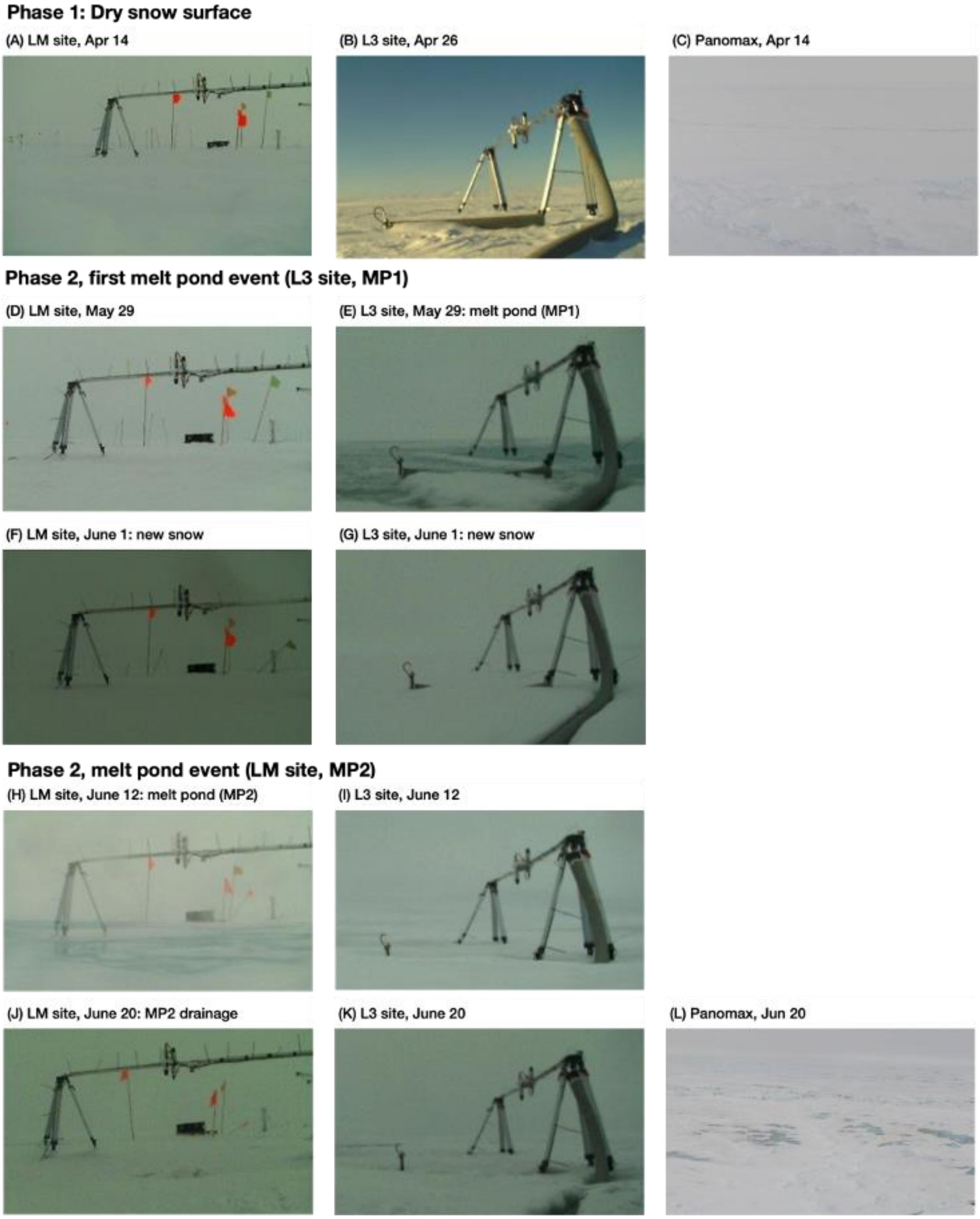
Phase 1: Dry snow surface
(A) LM site, Apr 14
(B) L3 site, Apr 26
(C) Panomax, Apr 14
Phase 2, first melt pond event (L3 site, MP1)
(D) LM site, May 29
(E) L3 site, May 29: melt pond (MP1)
(F) LM site, June 1: new snow
(G) L3 site, June 1: new snow
Phase 2, melt pond event (LM site, MP2)
(H) LM site, June 12: melt pond (MP2)
(I) L3 site, June 12
(J) LM site, June 20: MP2 drainage
(K) L3 site, June 20
(L) Panomax, Jun 20

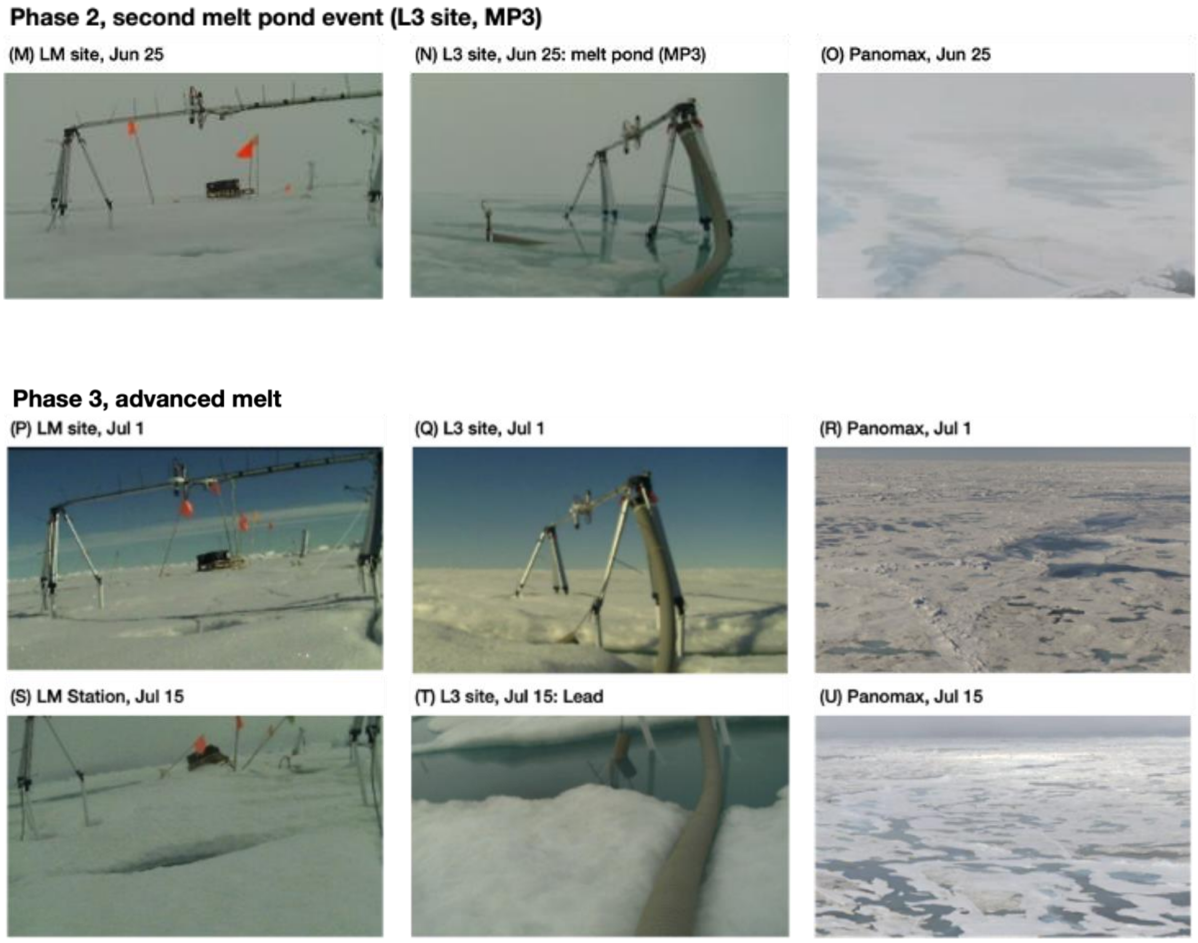

Figure 4. Surface conditions from April to July, 2020. Photos were taken by autonomous cameras at the LM and L3 site and from *Polarstern* (Panomax camera) monitoring the conditions of and around the radiation stations as labelled with the dates. Note that no photos from *Polarstern* are available for times when the vessel had to leave the floe for logistical reasons.

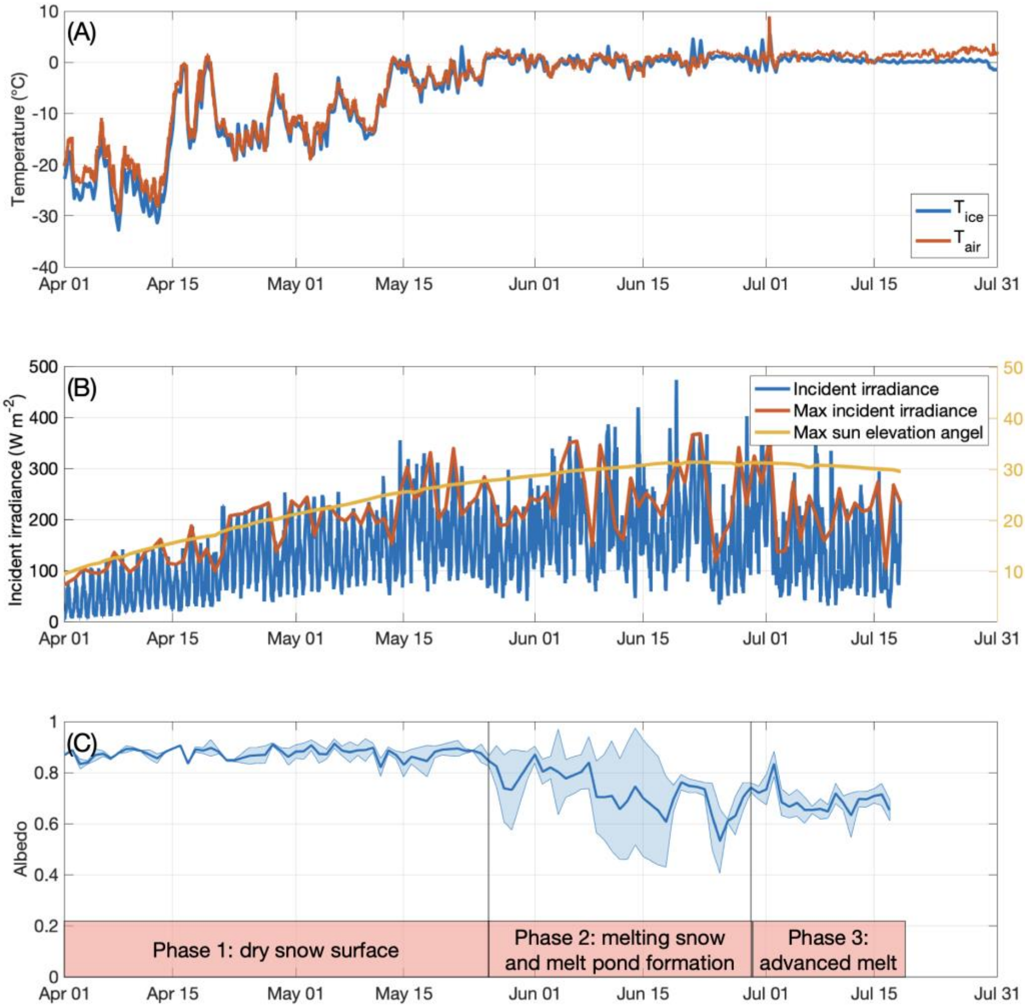

Figure 5. Surface evolution from April to July 2020. (A) Air and sea ice temperature from 2020M29 and 2019S94. (B) Incident solar irradiance from 2020R11. (C) Mean and standard deviation of total albedo from the 3 radiation stations at the LM, L3, and CO sites (2020R11, 2020R12, and 2020R14). The red-shaded areas mark the three phases.

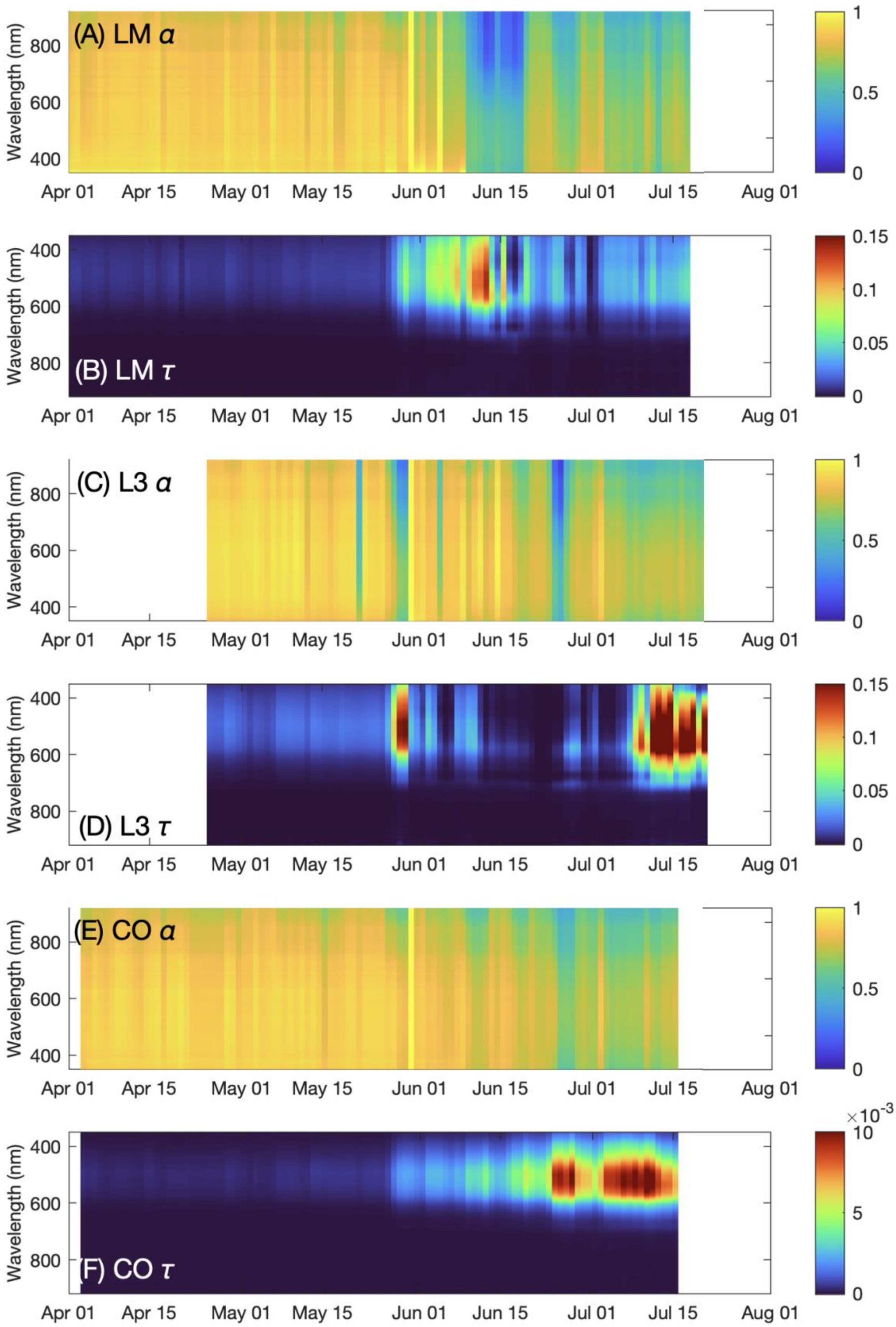
(A) LM α
Wavelength (nm)
400
600
800
Apr 01
Apr 15
May 01
May 15
Jun 01
Jun 15
Jul 01
Jul 15
Aug 01
0
0.5
1
(B) LM τ
0.15
0.1
0.05
(C) L3 α
(D) L3 τ
(E) CO α
(F) CO τ
×10^-3
10
5

788

Figure 6. Spectral albedo and transmittance of sea ice from 3 stations in spring/summer 2020. One spectrum is shown per day, from the measurement at the time of highest solar elevation. Results for each site are shown on two plates, one for spectral albedo (*α*) and one for spectral transmittance (*τ)* at (A+B) LM, (C+D) L3, and (E+F) CO. Note the different scale of transmittance for plate F.

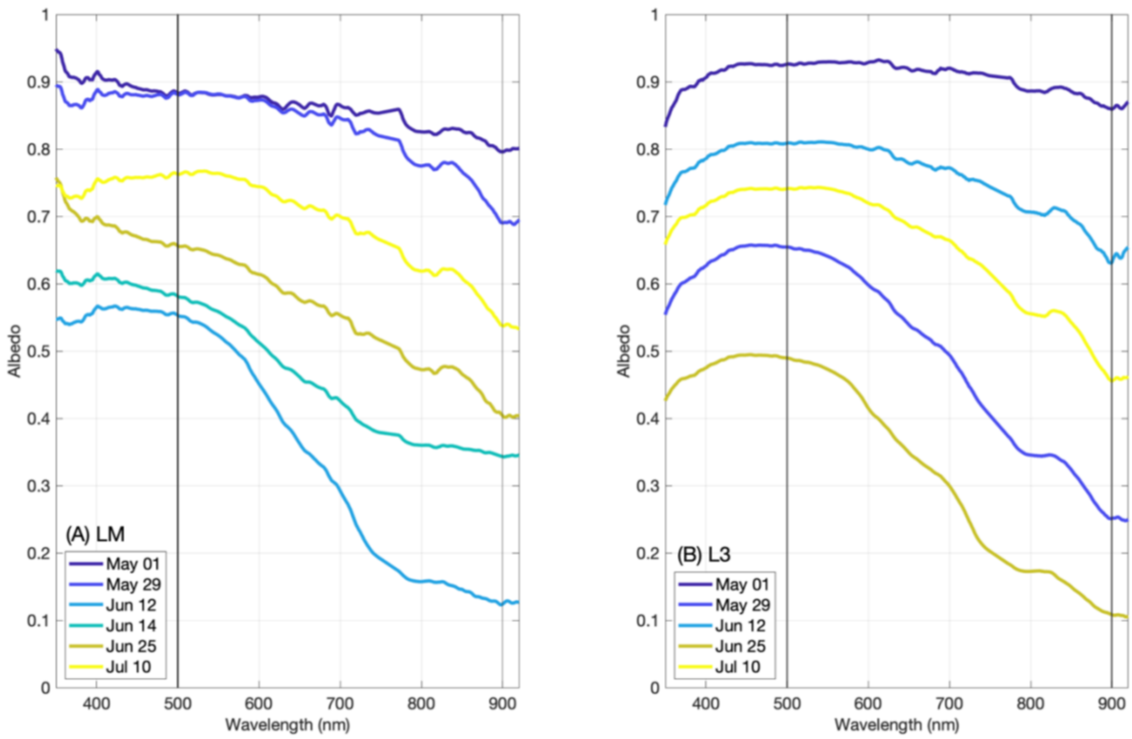

Figure 7. Albedo spectra for selected dates in spring/summer 2020. (A) LM and (B) L3 station. The solid vertical lines highlight the wavelengths of 500 nm and 900 nm, because of their relevance for the α(900)/ α(500) ratio (Figure 4D).

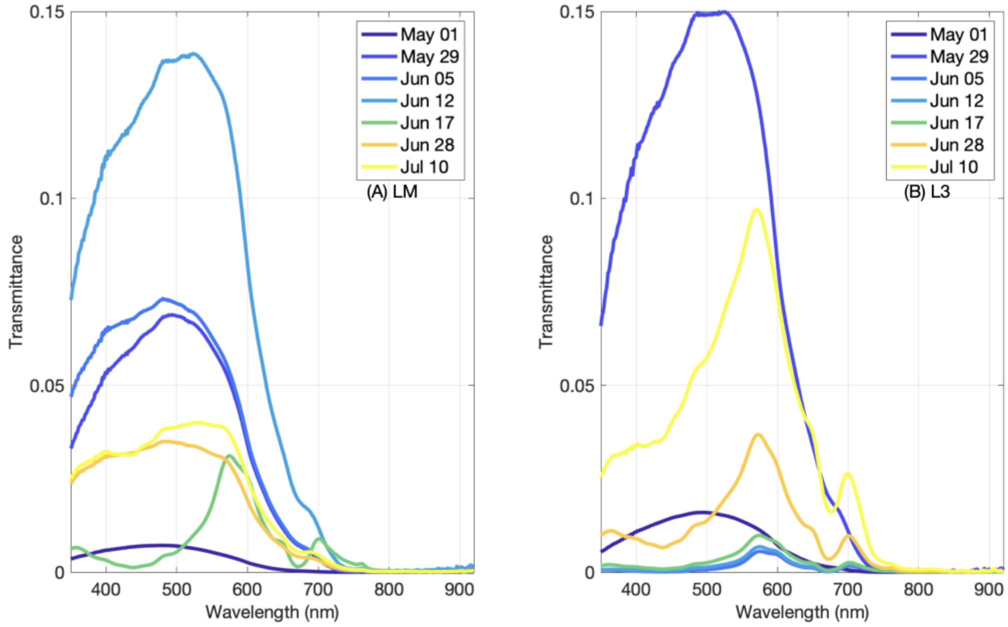

Figure 8. Transmittance spectra for selected dates in spring/summer 2020. (A) LM and (B) L3 station. The solid vertical lines highlight the wavelengths of 440 nm and 600 nm, because of their relevance for the *τ(600)/ τ(450)* ratio (Figure 4F). In addition, the wavelength of 670 nm is highlighted, representing the centre of absorption of Chlorophyll-a.

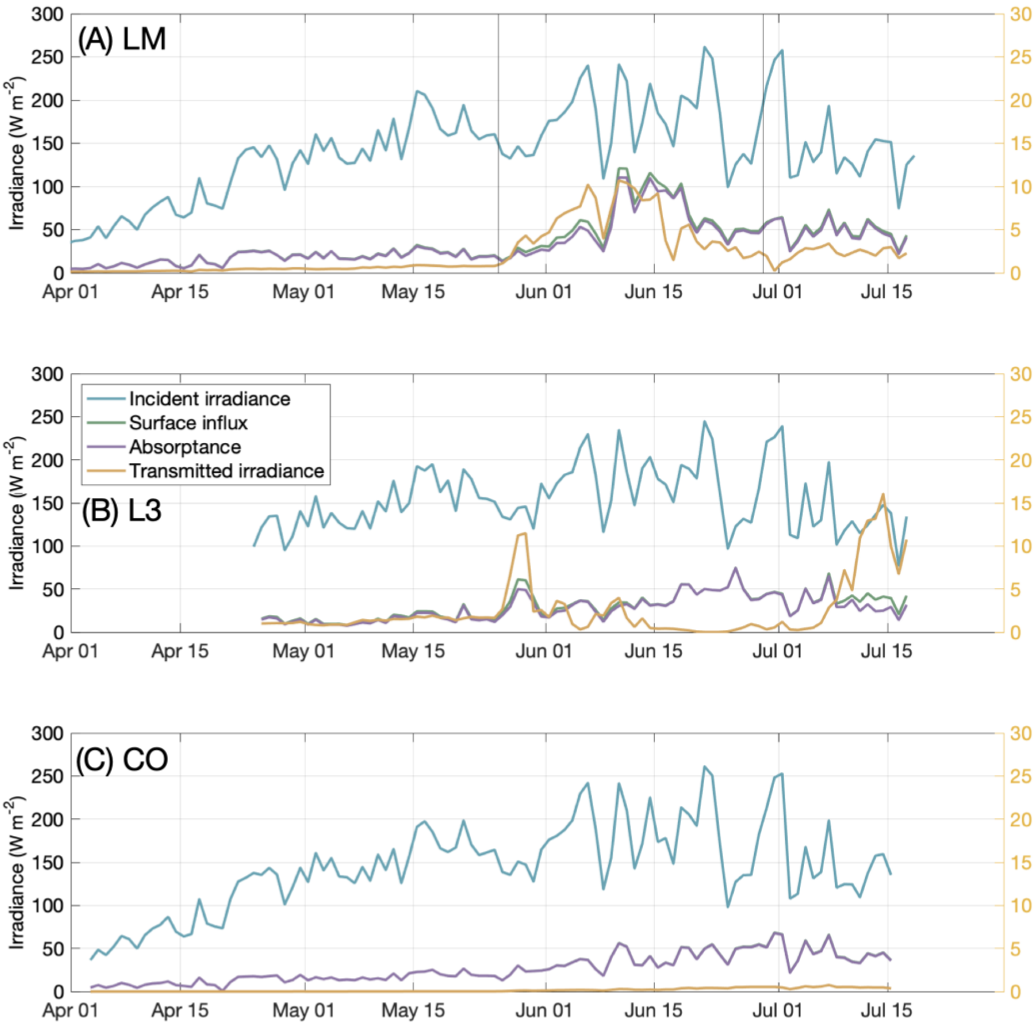

Figure 9. The seasonal evolution of the radiative fluxes of sea ice at different sites during spring/summer 2020. Daily mean of incident irradiance, flux into the surface, absorptance by sea ice plus the uppermost ocean, and transmitted irradiance into the ocean at (A) LM, (B) L3, and (C) CO. At panel A, the two black vertical lines indicated the melt onset (May 26) and stage of advanced melt and the formation of surface weathered layer (June 28).

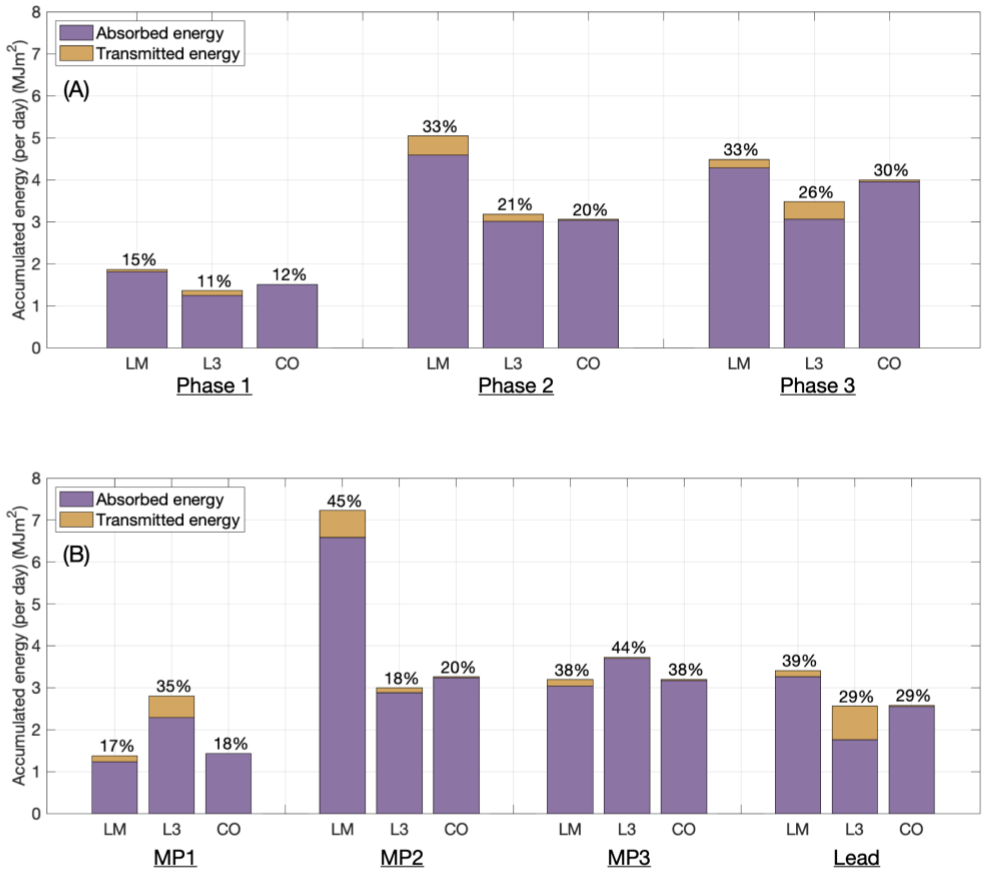

Figure 10. Daily mean of absorbed and transmitted irradiance at difference sites. (A) Integrated during Phase 1 (April 25 to May 26), Phase 2 (May 26 to June 29), and Phase 3 (June 30 to July 15). (B) Integrated over individual events: MP1: first ponding event at L3 site (May 26 to May 29), MP2: ponding event at LM site (June 4 to June 19), MP3: second ponding event at L3 site (June 25 to June 29), and lead formation near the L3 site (July 10 to July 15). The text above each bar shows the ratio of the energy deposition (total of absorbed and transmitted) to the mean solar incoming energy during each phase and event.

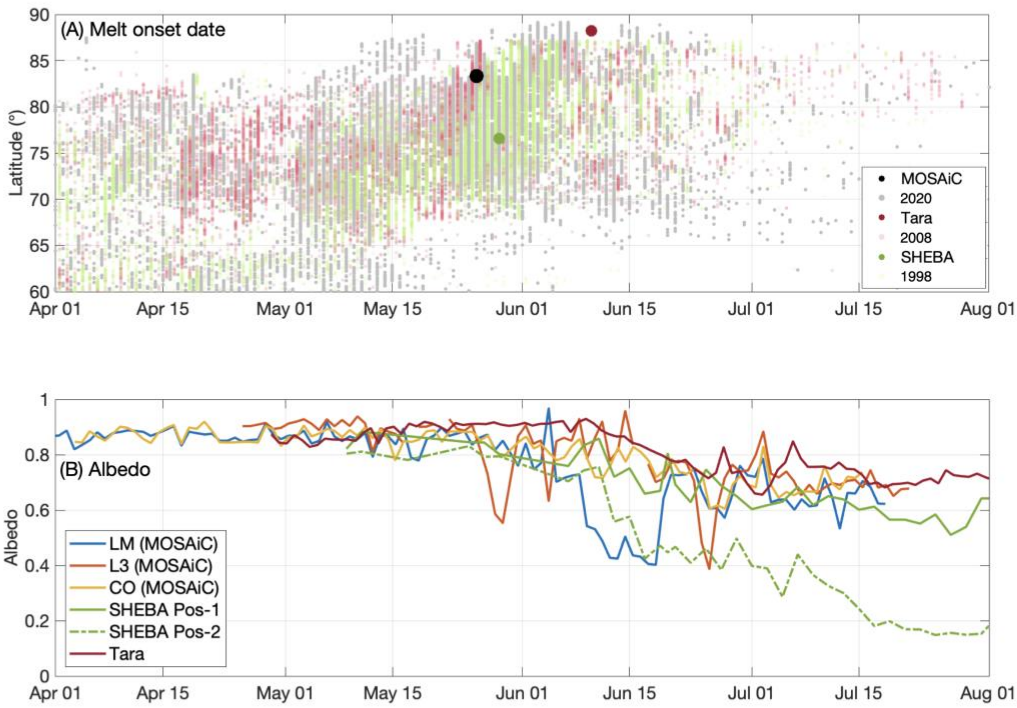

Figure 11. Surface evolution and melt onset date. (A) Melt onset from the MOSAiC, Tara (Nicolaus et al., 2010), and SHEBA (Perovich et al., 2002) expeditions. The melt onset date is acquired from SMMR (Scanning Multichannel Microwave Radiometer) (Anderson et al., 2019). (B) albedo measurements from the MOSAiC, Tara (Nicolaus et al., 2010), and SHEBA (Perovich et al., 2002) expeditions when transitioning into the melt season. The SHEBA albedo is extracted as 2 fixed positions (Pos-1 and -2) from the albedo line observation.